Tenth International Conference on Computational Fluid Dynamics (ICCFD10), Barcelona,Spain, July 9-13, 2018

ICCFD10-2018-100

A High-Order Kinetic Energy Conserving Scheme for Compressible Large-Eddy Simulation

F. Cadieux*, M. Barad**, and C. Kiris**
Corresponding author: francois.cadieux@nasa.gov

* Science & Technology, Moffett, CA, USA.
** NASA Ames Research Center, Moffett, CA, USA.

Abstract

Minimizing or controlling numerical dissipation is the key to realizing the promise of large-eddy simulation (LES): to produce results whose first order statistics agree with direct numerical simulation (DNS) at 1 to 10% of the computational cost. Whether LES is used to predict acoustic noise, transition from laminar to turbulent flow, or unsteady separated flows, the methodology hinges on the amount and location of dissipation added by numerics (in the case of implicit LES) or by a subgrid-scale (SGS) model (in the case of explicit LES) being just enough to account for the unresolved dissipative scales. A kinetic energy conserving compressible Navier-Stokes algorithm suitable for explicit LES is presented and implemented in the context of a Cartesian immersed boundary framework with adaptive mesh refinement. Results for standard benchmark cases such as isentropic vortex propagation, and the inviscid Taylor Green Vortex (TGV) showcase the methodology's ability to conserve kinetic energy. The level of agreement obtained for LES of the TGV at Reynolds number 1600, turbulent channel flow at Re_τ=180, and flow past a cylinder at $Re_D = 3900$, using this new approach demonstrates its ability to capture more physics at lower resolutions without the need for any limiters or artificial dissipation.

1 Introduction

NASA has called for an increase in computational fluid dynamics (CFD) prediction accuracy of 30% for separated and unsteady flows in its CFD 2030 vision [1]. Minimizing or controlling numerical dissipation in large-eddy simulation (LES) is one of the key advances that will help produce CFD predictions whose first order statistics recover those of DNS at 1 to 10% of the computational cost.

Numerical dissipation is introduced primarily in estimating the non-linear convective fluxes to stabilize otherwise only conditionally stable schemes and to deal with discontinuities in the solution (e.g. shocks, contact discontinuity, grid spacing disparities, etc). In incompressible flows, conservation of kinetic energy is guaranteed in space for central differencing, and in time with the use of symplectic time integrators: implicit methods that conserve quadratic invariants and are thus essentially reversible [2]. In all other methods, including commonly used second-order accurate finite volume methods, the kinetic energy loss is proportional to the level of under-resolution of the flow and the overall order of accuracy of the scheme, which is often driven by the non-linear convective fluxes and approximations used therein. Whether LES is used to predict acoustic noise, transition from laminar to turbulent flow, or unsteady separated flows, the methodology hinges on the amount and location of dissipation added by numerics (in the case of implicit LES) or by a subgrid-scale (SGS) model (in the case of explicit LES) being just enough to account for the unresolved dissipative scales. However, recent work has shown that numerical dissipation can be quantified [3], and it was found to be larger than what an explicit SGS model would provide in one commercial and two academic Navier-Stokes solvers (two were compressible, and one incompressible) [4, 5]. Many LES suffer from excessive dissipation, to which there are only three possible remedies:

1. Increase the mesh resolution in key areas,

2. Decrease or remove contribution from SGS model,

3. Modify the numerics to use as little dissipation as possible.

Identifying where to refine the mesh to improve LES results is still an area of active research: it requires either expert knowledge in CFD, or long enough integration times to post-process indicators of under-resolution such as the ratio of resolved to modeled turbulent kinetic energy. Moreover, unless the grid refinement is done globally and consistently in all directions, the obtained results may not improve monotonically given a particular metric of interest (e.g. capturing the skin friction on an airfoil at moderate to high angles of attack). If dissipation provided by the numerical scheme is comparable or larger than what modern SGS models like the dynamic Smagorinsky and σ models provide, reducing or removing the contribution from the SGS model might be beneficial, but it may also jeopardize agreement with the log law of the wall in wall-bounded flows. Due to the known difficulties of the first two options, we explore the avenue of removing numerical dissipation altogether for smooth problems, and adding dissipation only where discontinuities in the solution or the grid occur.

Recent work has shown that it is possible to conserve kinetic energy in space and in time for the compressible Navier-Stokes equations by carefully re-arranging terms and using a density-weighted symplectic time integrator [6, 7]. In this work, we modify the kinetic energy conserving scheme of Brouwer *et al.*[7] and extend it to a Cartesian immersed boundary approach implemented in the Launch, Ascent, and Vehicle Aerodynamics (LAVA) framework [8].

First, the proposed kinetic energy conserving algorithm is detailed in section 2. Its implementation in the LAVA Cartesian immersed boundary framework with adaptive mesh refinement (AMR) [8] is described in section 3. Then we present results that demonstrate the new algorithm's ability to conserve mass, momentum, internal energy, and kinetic energy both in space and in time in section 4. Finally, we show LES results for the Taylor Green Vortex problem at $Re = 1600$, turbulent channel flow at $Re_\tau = 180$, and flow past a cylinder at $Re_D = 3900$.

2 Numerical Methods

Brouwer *et al.* solve the Navier-Stokes equation in conservative finite difference form (no interpolation to faces) for $\left\{\sqrt{\rho}, \sqrt{\rho}u_i, \sqrt{p}\right\}$ to enable conservation of kinetic energy in time without the added expense of computing square roots [6], and use the state equation to eliminate internal energy [7]. To keep the structure of the equations more general and admit different equations of state (e.g. non-ideal gas) while maintaining kinetic energy conservation in time, we solve for the variables $\left\{\sqrt{\rho}, \sqrt{\rho}u_i, \sqrt{\rho e}\right\}$. Brouwer *et al.* note that their proposed formulation suffers from decoupling between the convective and viscous terms due to the use of repeated first derivatives, which are effectively blind to grid level oscillations. They solve this problem with the use of high-order conservative filtering [7]. Here we use the product rule to expand all dissipation terms to combinations of first, pure and mixed second derivatives to avoid the problem of decoupling altogether and eliminate the need for filtering. Another important improvement is the inclusion of a consistent skew-symmetric total energy convection term on top of the skew-symmetric momentum terms. This allows the scheme to be stable without any dissipation mechanism for low Mach number periodic flows at any Reynolds

number [9]. With these changes, the Navier-Stokes equations are solved in the following form:

$$\frac{\partial\sqrt{\rho}}{\partial t} = -\frac{1}{2\sqrt{\rho}}\left[\frac{\partial}{\partial x_j}(\rho u_j)\right], \tag{1}$$

$$\begin{aligned}\frac{\partial\sqrt{\rho}u_i}{\partial t} = \frac{1}{\sqrt{\rho}}\Bigg[&-\frac{1}{2}\left(\frac{\partial}{\partial x_j}(\rho u_j u_i) + \rho u_j\frac{\partial u_i}{\partial x_j}\right) - \frac{\partial p}{\partial x_i} \\ &+ \frac{\partial\mu}{\partial x_j}\left(\frac{\partial u_i}{\partial x_j} + \frac{\partial u_j}{\partial x_i}\right) + \frac{\partial\beta}{\partial x_j}\frac{\partial u_k}{\partial x_k}\delta_{i,j} \\ &+ (\mu(1+\delta_{i,j}) + \beta\delta_{i,j})\frac{\partial^2 u_i}{\partial x_j^2} + (\mu+\beta)(1-\delta_{i,j})\frac{\partial^2 u_j}{\partial x_i x_j}\Bigg], \quad i = 1,2,3\end{aligned} \tag{2}$$

$$\begin{aligned}\frac{\partial\sqrt{\rho}e}{\partial t} = \frac{1}{\sqrt{\rho}}\Bigg[&-\frac{1}{2}\left(\frac{\partial}{\partial x_j}(\rho e u_j) + \rho u_j\frac{\partial e}{\partial x_j}\right) - \frac{\partial p u_j}{\partial x_j} + u_i\frac{\partial p}{\partial x_i} \\ &+ \frac{\partial u_i}{\partial x_j}\left(\mu\left(\frac{\partial u_i}{\partial x_j} + \frac{\partial u_j}{\partial x_i}\right) + \beta\frac{\partial u_k}{\partial x_k}\delta_{i,j}\right) + \frac{\partial\kappa}{\partial x_j}\frac{\partial T}{\partial x_j} + \kappa\frac{\partial^2 T}{\partial x_j^2}\Bigg]\end{aligned} \tag{3}$$

$$\frac{\partial\sqrt{\rho}Y_i}{\partial t} = \frac{1}{\sqrt{\rho}}\left[-\frac{1}{2}\left(\frac{\partial}{\partial x_j}(\rho u_j Y_i) + \rho u_j\frac{\partial Y_i}{\partial x_j}\right)\right], \quad i = 1,2,3 \tag{4}$$

where the variables take on their usual meanings of density ρ, velocity in the Cartesian directions $[u_1, u_2, u_3]$, pressure p, temperature T, internal energy e, and mixture mass fraction Y. No assumptions have been made regarding the particular equation of state that relates primary variables to conserved variables. This formulation has several advantages. When discretized with derivative matrices that have the property $D = -D^T$, like the 6^{th} order explicit central finite differences used in this work, along with a symplectic time integrator that preserve quadratic invariants (e.g. implicit Runge-Kutta schemes with Gauss quadrature), this formulation guarantees conservation of kinetic energy in space and in time (in the absence of viscosity, and on periodic grids) [6, 7]. This formulation also has advantages when explicit time integrators are used in that it does not suffer from the spurious transfer of kinetic energy to internal energy typically seen in compressible flux-based finite difference schemes for turbulent flows at low to moderate Mach numbers [10, 9]

For LES, the σ model [11] with the dynamic procedure to determine C_σ [12] is currently implemented as a modern starting point because it provides minimal dissipation away from turbulent regions. The computed SGS viscosity μ_{SGS} is added to the viscosity μ, which in turn affects thermal conductivity in the usual way $\kappa = c_P(\mu + \mu_{SGS})/Pr$, where Pr is the Prandtl number and c_P is the specific heat coefficient at constant pressure.

3 Implementation Details

The proposed kinetic energy conserving algorithm (KECons) outlined in section 2 eschews traditional flux formulations while maintaining conservation properties [7]. This simplifies its implementation in that a single subroutine needs to be maintained and optimized to increase the computational performance of the algorithm: a flexible stencil operator that can perform derivatives of varying orders and accuracy. It also allows for more direct estimates of the scheme's truncation, dissipation and dispersion error as the confounding effects of interpolation are removed. This comes at the cost of a higher operation count per iteration. However, with current and future architectures that are memory bound, increasing the number of operations between communication cycles while decreasing the working memory set can increase parallel efficiency.

Although the scheme is stable for most low Mach number flows at any Reynolds number on periodic grids, the application of non-periodic boundary conditions can break this provable stability. LAVA implements boundary conditions by filling in values on the three layers of domain ghost cells. However, this can create problems, for example, when the outflow boundary sees vorticity or a pressure wave. The boundary condition applied on the ghost cells may not be a good solution of the Navier-Stokes equations, and thus vortical and pressure waves may reflect back into the domain. To minimize this effect without implementing complex

boundary conditions that may work well for one flow type but fail in another, two options are available: sponge regions where a body force returns the flow to a known solution smoothly as it gets closer to the domain boundary [13], or smoothly adding high order artificial dissipation (upwinding) [14] near the domain boundary. Both approaches are implemented and are effective in reducing reflections to acceptable levels.

Complex and potentially moving geometry is handled by LAVA's immersed boundary framework. The second-order ghost cell method (GCM) of Mittal *et al.*[15] is used to fill in primary variables for all in-body neighbors to fluid cells. To guarantee kinetic energy conservation, the order of accuracy of the derivatives used near the geometry is dropped smoothly from sixth to fourth, and from fourth to second order explicit centered differences such that no stencil requires data beyond the single layer of ghost cells inside the body determined from the GCM. Summation-by-parts (SBP) near-boundary operators were also tested to perform energy-stable order of accuracy reduction near geometry. Little difference between the two approaches was observed in practical applications thus far. The SBP approach does display slightly higher levels of error in method of manufactured solutions (MMS) tests, and does require wider stencils near the boundary and so it was not pursued further. The choice of GCM and order of accuracy reduction near the geometry does lead to some non-smooth (stair-step) behavior for severely under-resolved geometry, but it has not caused numerical instability so far. The SBP operators did not visibly help to smooth out the solution for under-resolved geometry. In the future, higher order SBP-based immersed boundary methods with simultaneous approximation terms (SAT) [16] may be explored to increase the effective resolution of the scheme next to the geometry. The ghost-in-fluid method [17] is used to handle thin subgrid scale geometry like airfoil trailing edges and thin rotor blades.

Adaptive mesh refinement (AMR) is one of the most important enabling technologies for Cartesian approaches when dealing with problems that have a wide range of scales. The methodology implemented in LAVA creates patches where the cell sizes are recursively decreased by a factor of two in an isotropic fashion. LES has been shown to be very sensitive to grid quality and stretching. So this instantaneous stretching by a factor of two in all directions creates an effective boundary condition for the fine-to-coarse transition, which can result in the reflection of pressure and vortical waves. In order to avoid reflections at fine-to-coarse interfaces, the same high order artificial dissipation (upwinding) as is used at domain boundaries is used here for points adjoining the interface – the approach is akin to that of Pantano *et al.*[18]. Designing a better AMR interface that does not break conservation of kinetic energy locally, perhaps inspired by overset SBP operators and simultaneous approximation terms [19], will be a topic of future research.

4 Results

4.1 Method of Manufactured Solutions

The proposed kinetic energy conserving algorithm (KECons) in some ways increases the complexity of the solver and so it is important to demonstrate that we obtain the expected spatial convergence rate. The method of manufactured solutions (MMS) is used to provide an initial condition for which the right-hand-side (RHS) operator can be computed analytically. This capability has been integrated into the LAVA framework for arbitrary initial conditions using the complex step derivative method.

First we test the implementation for the Euler equations without geometry, then the viscous Navier-Stokes where the viscosity is set to 10^{10}, and finally we repeat the first two cases with under-resolved spheres present in the domain which are handled with the GCM (see figure 1). To obtain convergence rates, initial conditions for p, u, v, w, T are set to constants plus a sinusoidal functions in each Cartesian direction with a different wavelength for each primary variable, and the RHS is obtained for 3 different resolutions where the mesh size is halved every time. The exact boundary conditions from the given initial condition fields are imposed on the domain boundary ghost cells and inside the geometry if present.

The spatial convergence rates of the convective operators with and without geometry for KECons are compared to the more mature and well-tested 6^{th} order weighted essentially non-oscillatory (WENO6) with optimal weights in table 1. This becomes the limiting factor for its convergence. KECons and WENO6 (with optimal weights) both display the expected 6^{th} order convergence of their error with respect to the exact solution for the Euler equations without geometry. Absolute error magnitudes are comparable for KECons and WENO6 for the mass equation, their momentum lines lie on top of each other, and their energy equation errors are also very close with WENO6 taking a small lead. This could be due to the

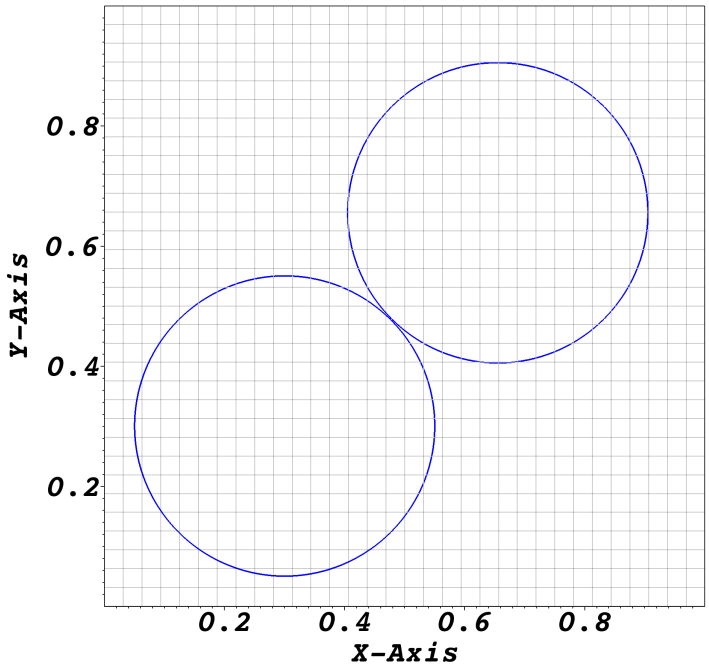

Figure 1: Cut of the two spheres in the domain used for MMS tests with geometry and the starting mesh (before any refinement).

transformation to characteristic space before the WENO interpolation is performed (e.g. the initial conditions may be smoother in characteristic space for the energy equation). Despite the greater number of individual derivative operations in KECons, as in all the skew-symmetric terms for example, which each have errors that are correlated and may be additive in the KECons algorithm, its error levels are almost identical to WENO6. This cannot be attributed to the skew-symmetric terms mitigating aliasing error in this MMS test because the wavelengths of the sinusoidal initial conditions are large – this is necessary for the schemes to be in the asymptotic region of convergence.

Table 1: L_∞ norm of the discretization error obtained from inviscid MMS without geometry. Convergence rates are shown in parenthesis.

Mesh	**Mass**		**Momentum**		**Total Energy**	
	WENO6	KECons	WENO6	KECons	WENO6	KECons
m0	3.6E-08	3.3E-08	2.6E-06	2.6E-06	8.4E-04	1.3E-03
m1	5.2E-10 (6.11)	5.3E-10 (5.96)	4.2E-08 (5.98)	4.1E-08 (5.99)	6.1E-06 (7.11)	2.1E-05 (5.97)
m2	8.2E-12 (5.98)	8.3E-12 (5.99)	6.7E-10 (5.98)	6.5E-10 (5.99)	9.9E-08 (5.94)	3.3E-07 (5.99)

Table 2: L_∞ norm of the discretization error obtained from inviscid MMS with two spheres close together as seen in figure 1. Convergence rates are shown in parenthesis.

Mesh	**Mass**		**Momentum**		**Total Energy**	
	WENO6	KECons	WENO6	KECons	WENO6	KECons
m0	1.9E-02	7.0E-05	4.4E-01	4.0E-02	1.3E+03	6.2E+00
m1	1.0E-02 (0.89)	1.8E-05 (2.01)	2.1E-01 (1.03)	1.0E-02 (2.00)	6.7E+02 (0.97)	1.5E+00 (2.01)
m2	5.0E-03 (1.00)	4.4E-06 (2.01)	1.1E-01 (1.02)	2.5E-03 (1.99)	3.4E+02 (0.98)	3.8E-01 (2.00)

Two spheres of diameter 1 are introduced in the MMS domain with a very narrow spacing between them for the case with geometry (see figure 1). This creates regions of concave curvature, which is seen as a concave corner until the finest refinement level where one cell lies between the spheres. This is a particularly difficult problem for WENO6 which drops to first order in the concave corner region as shown in figure 2. In contrast, we observe that KECons has strong second order convergence when dealing with under-resolved geometry.

Thanks to the way the viscous dissipation terms are decomposed and discretized in KECons, sixth order convergence is easily achieved for viscous Navier-Stokes without geometry as demonstrated in figure 3. Discretizing the viscous terms to higher order in flux form is significantly more difficult and can lead to numerical instability, so the WENO implementation utilizes a standard second order discretization. It reaches its expected convergence rate in the viscous case without geometry (figure 3), and with geometry (figure 4) because the way viscous terms are computed is not affected by geometry due to the availability of the in-body ghost cells. KECons similarly display second order convergence for the viscous Navier-Stokes with geometry. This successfully demonstrates the ability of KECons to reach the expected convergence rate from its discretization order of accuracy for the full Navier-Stokes with geometry.

Table 3: L_∞ norm of the discretization error obtained from MMS for the Navier-Stokes equations with $\mu = 10^{10}$. Convergence rates are shown in parenthesis.

Mesh	**Mass**		**Momentum**		**Total Energy**	
	WENO6	KECons	WENO6	KECons	WENO6	KECons
m0	3.7E-08	3.3E-08	1.3E+08	3.0E+04	7.8E+12	1.2E+09
m1	5.3E-10 (6.12)	5.3E-10 (5.96)	3.2E+07 (1.99)	4.7E+02 (5.98)	2.0E+12 (1.99)	1.9E+07 (5.98)
m2	8.3E-12 (5.98)	8.3E-12 (5.99)	7.9E+06 (2.00)	7.6E+00 (5.96)	4.9E+11 (2.00)	3.1E+05 (5.95)

Table 4: L_∞ norm of the discretization error obtained from MMS for the Navier-Stokes equations with $\mu = 10^{10}$ and with two spheres close together (see figure 1). Convergence rates are shown in parenthesis.

Mesh	**Mass**		**Momentum**		**Total Energy**	
	WENO6	KECons	WENO6	KECons	WENO6	KECons
m0	1.9E-02	7.0E-05	1.2E+08	1.3E+08	7.7E+12	3.6E+12
m1	1.0E-02 (0.89)	1.8E-05 (2.01)	3.1E+07 (1.99)	3.2E+07 (1.97)	2.0E+12 (1.99)	8.6E+11 (2.07)
m2	5.0E-03 (1.01)	4.4E-06 (2.01)	7.9E+06 (1.99)	8.1E+06 (1.99)	4.9E+11 (2.00)	2.1E+11 (2.02)

4.2 Isentropic Vortex Propagation

To demonstrate the conservation properties of the proposed kinetic energy conserving scheme (KECons) in space and in time, the two-dimensional nonlinear Euler equations are solved for the isentropic vortex propagation problem. The domain for this simulation spans $[-1, 1]$ in x and y and the problem admits exact

solutions of the form:

$$\begin{bmatrix} \rho(\vec{x},t) \\ u(\vec{x},t) \\ v(\vec{x},t) \\ p(\vec{x},t) \end{bmatrix} = \begin{bmatrix} \rho_r(r) \\ U_0 - u_r(r)\sin(\theta) \\ V_0 + u_r(r)\cos(\theta) \\ p_r(r) \end{bmatrix} \tag{5}$$

where

$$r = \sqrt{(x-U_0t)^2 + (y-V_0t)^2}, \text{ and } \theta = \arctan(y/x) \tag{6}$$

$$u_r(r) = \frac{U'_{\max}}{b} r e^{\frac{1}{2}(1-\frac{r^2}{b^2})} \tag{7}$$

$$\rho_r(r) = \left(1 - \frac{1}{2}(\gamma-1)U'^2_{\max} e^{\frac{1}{2}(1-\frac{r^2}{b^2})}\right)^{\frac{1}{\gamma-1}} \tag{8}$$

$$p_r(r) = \frac{1}{\gamma}\rho_r^\gamma \tag{9}$$

The initial conditions are set as follows: $U_0 = 0.5$, $V_0 = 0$, $U'_{\max} = 0.5U_0$, $b = 0.2$, with $\gamma = 1.4$, and $c_p = 2.5$. This gives a baseline density and temperature of 1, with pressure at 0.714253, and Mach number 0.5. One flow-through time (FT) or the time necessary for the vortex to be convected around the domain back to its original position is 4 time units, and results are presented for 10 FT or, equivalently, 40 time units as was done in previous work with the LAVA framework [20]. The domain is discretized with 32 uniformly spaced points in each direction, and time integration is performed with the classic fourth-order Runge-Kutta (RK4) scheme with a relatively small time step $\Delta t = 0.01$ to keep time integration errors as minimal as possible compared to spatial discretization errors, which gives a CFL number of roughly 0.28 . KECons does not require any stabilization mechanism for this problem because the solution is smooth and because of the algorithm's strong skew-symmetric nature. In contrast, finite difference algorithms in strong conservation form (e.g. WENO6 with optimal weights) require stabilization for this problem, and otherwise quickly become numerically unstable. This is because WENO6 collapses to a sixth-order central scheme with no dissipation when used with optimal weights. So only results for WENO6 with non-linear weights are shown from here on out. The contours of vorticity after 10 FT for KECons and WENO6 (with non-linear weights) are compared to the exact solution in figure 2. From this figure, the dissipative nature of the WENO approach is already visible: the level of vorticity at the center of the vortex has diminished and now occupies a much smaller area. Figure 3 shows the recovery of the pressure at the center of the vortex and the kinetic energy loss for KECons compared to two common high-order finite difference schemes: WENO6, and 6^{th} order central differences with 5^{th} order scalar-based artificial dissipation with $\epsilon_6 = 0.001$ (Central6). KECons here shows the least deviation from the exact solution, with WENO6 a close second. However, it is clear that WENO6 starts to lose kinetic energy from the start, whereas the KECons level of kinetic energy remains constant.

A fully implicit Runge-Kutta (IRK) time integration capability was developed to test kinetic energy conservation in time at higher CFL numbers. For this purpose, we tested the symplectic Gauss quadrature of fourth order (Gauss4) with a simple explicit fixed-point sub-iteration technique with linear convergence. The obtained convergence rate is sub-optimal, but this approach has the advantage that it doesn't require the creation and approximate solution of a full non-linear system of equations. The results shown in figure 4 were somewhat disappointing when the total time to solution was taken into account. The explicit RK4 simulations with $\Delta t = 0.01$ reached a total integration time of 40 time units in approximately 8 seconds when parallelized on 44 Message Passing Interface (MPI) threads on a desktop workstation. The Gauss4 simulation with the same time step and a convergence tolerance of 1×10^{-10} took about 30 seconds to reach 40 time units with the same number of MPI threads on the same workstation. Both produce the same level of solution error (e.g. deviation from exact pressure distribution), and conservation error (e.g. kinetic energy loss). It is clear that comparing RK4 to Gauss4 for the same time step and this tight convergence tolerance, the ratio of solution error to computational time is in favor of RK4. There is however some advantage to the Gauss4 approach at higher CFL numbers. The Gauss4 simulation with the larger time step $\Delta t = 0.04$ corresponding to a CFL number of 1.1 and the same tolerance also took approximately 30 seconds, but did not produce noticeably more error in the solution. This is because for the 40 time units of interest, time

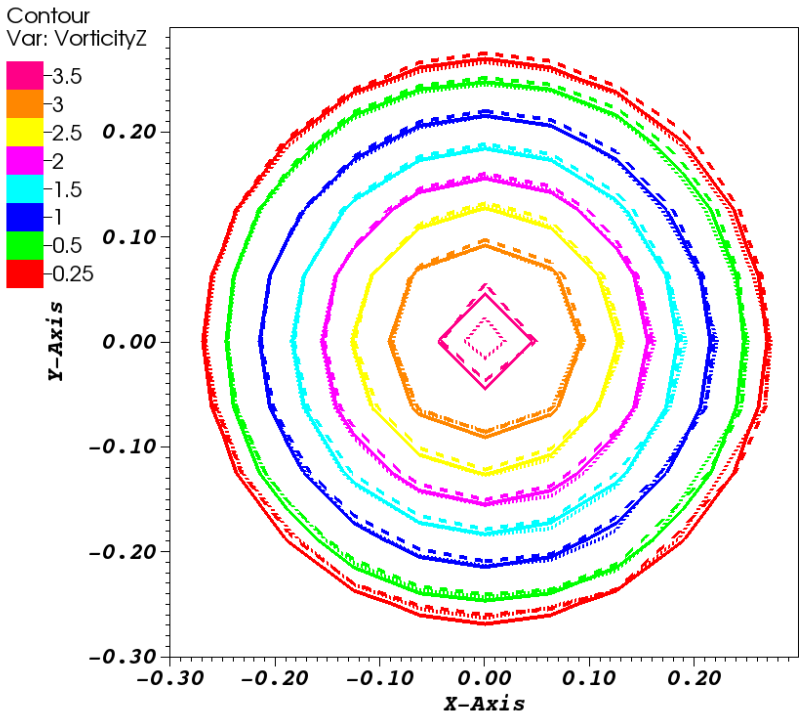

Figure 2: Contours of vorticity for isentropic vortex propagation problem after 10 flow-through times using WENO6 (dots) and KECons (dashes) versus exact solution (lines).

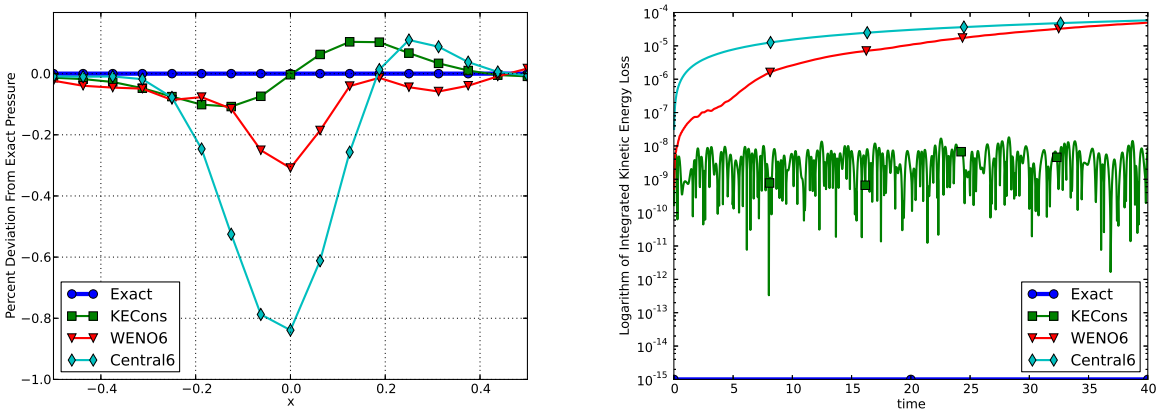

(a) $(p_{\text{exact}} - p)/p_{\text{exact}} \times 100\%$

(b) $\log(\int_\Omega K_{\text{exact}} \mathrm{d}V - \int_\Omega K \mathrm{d}V)$, where $K = \frac{1}{2}\rho u_i u_i$

Figure 3: Comparison of inviscid isentropic vortex propagation results for different high order finite difference schemes after 10 flow-through times.

integration error accumulates: the larger the CFL number, the fewer instances where error is accumulated. In order for Gauss4 to complete the simulation in the same wall time as the RK4 algorithm (8 seconds), the number of sub-iterations have to be limited to 10, which produces kinetic energy conservation error levels 4 orders of magnitude larger as shown in figure 4b. The nature and distribution of error in the solution for pressure is also significantly affected, in a potentially dangerous way: instead of recovering, the pressure at the

center of the vortex further decreases. This is consistent with past accounts where high sensitivity to implicit residual convergence criteria were observed for implicit Runge-Kutta schemes with Gauss quadratures [21]. The Gauss4 scheme considered in this isotropic Cartesian setting will thus only become advantageous for nearly incompressible flows, or when an accurate and well-optimized Newton-Krylov solver is implemented along with an accurate left-hand-side to make the overall computational time to solution competitive with RK4.

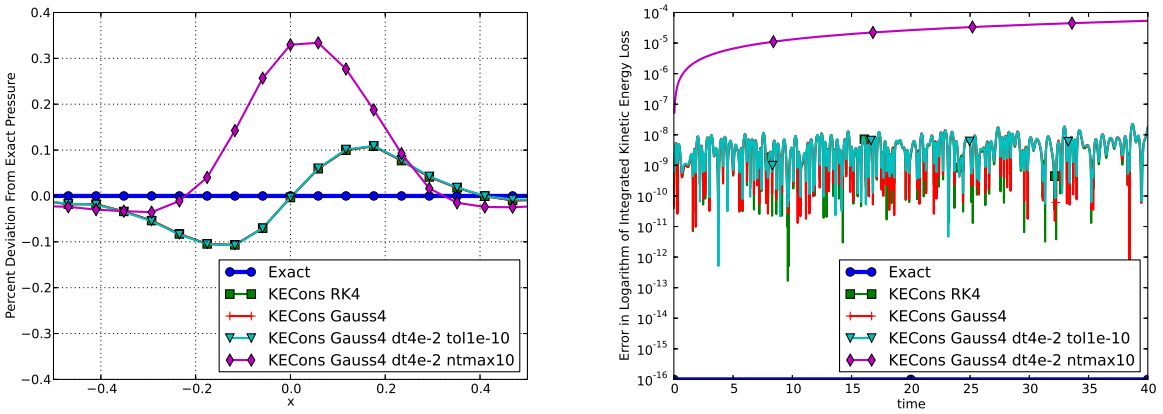

(a) $(p_{\text{exact}} - p)/p_{\text{exact}} \times 100\%$

(b) $\log(\int_\Omega K_{\text{exact}} \mathrm{d}V - \int_\Omega K \mathrm{d}V)$, where $K = \frac{1}{2}\rho u_i u_i$

Figure 4: Comparison of inviscid isentropic vortex propagation results for KECons with explicit RK4 (squares), Gauss4 (crosses), Gauss4 using a 4 times larger time step (triangles), and Gauss4 using a 4 times larger time step and a limit of 10 sub-iterations (diamonds).

4.3 Inviscid Taylor-Green Vortex

The inviscid Taylor-Green Vortex (TGV) is a useful problem to demonstrate numerical stability and conservation of kinetic energy in a highly under-resolved turbulent problem. The flow field is initialized as follows:

$$
\begin{aligned}
u &= V_0 \sin(\frac{x}{L}) \cos(\frac{y}{L}) \cos(\frac{z}{L}), \\
v &= -V_0 \cos(\frac{x}{L}) \sin(\frac{y}{L}) \cos(\frac{z}{L}), \\
w &= 0, \\
p &= p_0 + \frac{\rho_0 V_0^2}{16} \left(\cos(2\frac{x}{L}) + \cos(2\frac{y}{L})\right) \left(\cos(2\frac{z}{L}) + 2\right), \textit{and} \\
T &= T_0.
\end{aligned}
$$

The ideal gas law is assumed with $\gamma = 1.4$, and $c_p = 3.5$. The dynamic viscosity μ_0 is set to zero. The temperature T_0 is chosen such that the Mach number $M_0 = V_0/c_0 = 0.1$, where c_0 is the speed of sound. The domain is discretized using 32 points in each Cartesian direction. The time step is set to $\Delta t = 0.0014$, which gives a CFL number near 0.5. The simulation is run for 20 non-dimensional time units $t_c = L/V_0$. For the inviscid case, it is accepted that the total kinetic energy in the volume should remain constant whereas the enstrophy should increase exponentially. No subgrid-scale models are used in this problem for any of the schemes tested. All simulations were integrated explicitly in time using RK4 unless otherwise noted.

Figure 5 demonstrates that even for severely under-resolved flow, the proposed approach is numerically stable and conserves kinetic energy almost exactly, whereas all other approaches cause the kinetic energy to decay rather rapidly. WENO6 with is able to delay adding numerical dissipation for the longest, whereas the Central6 scheme has some level of numerical dissipation from the very start by design. However, once

the smoothness indicator is tripped, WENO6 provides a higher dissipation rate than Central6. For this reason, WENO6 tracks the expected increase in enstrophy the best for $t < 3$, but reaches a lower maximum enstrophy than Central6. KECons results agree with theoretical predictions for $t < 8$, after which the size of vortical structures generated becomes comparable to what the derivative operator can resolve on this mesh. Subsequently, the rate of enstrophy growth decreases significantly beyond $t = 10$. This is consistent with what theory predicts: the smallest resolved scales will accumulate energy and start interacting with the larger scales until all energy is equi-partitioned between all resolved wavenumbers.

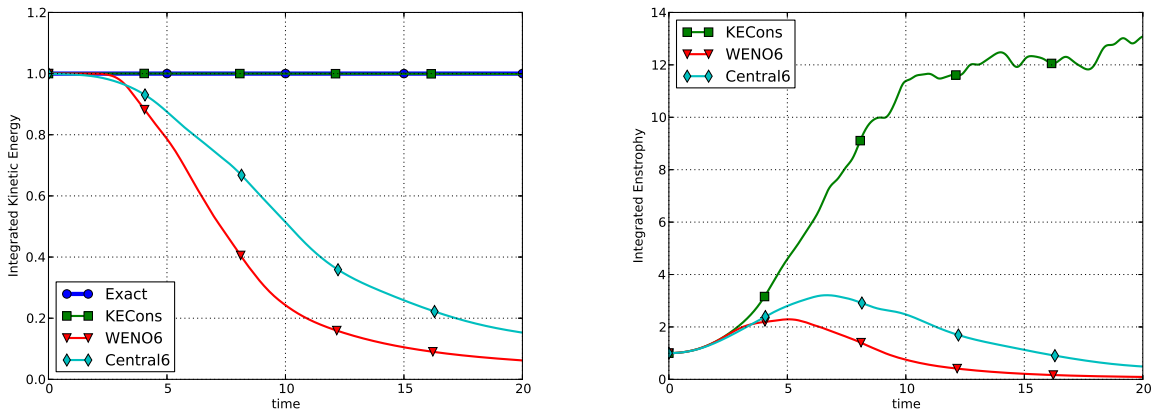

(a) Non-dimensional integrated kinetic energy

(b) Integrated enstrophy

Figure 5: Comparison of inviscid Taylor-Green vortex results for different high order finite difference schemes over 20 flow-through times.

4.4 Taylor-Green Vortex

The Taylor-Green Vortex (TGV) at $Re = 1600$ is a well-established problem for which benchmark DNS data exists. The problem description is identical to that described in section 4.3, with the exception that the dynamic viscosity is set to $\mu_0 = 1/Re$. The goal is to predict the correct rate of dissipation at the lowest resolution possible as the flow transitions from laminar to turbulent and the relevant length scales become smaller and smaller. Time integration is performed again with explicit RK4 with a CFL of 0.5 for all computations.

Figure 6 demonstrates the strength of the KECons approach. KECons with the dynamic σ SGS model produces a kinetic energy evolution and dissipation rate that is in excellent agreement with the DNS benchmark. KECons predicts the peak dissipation almost exactly at resolutions beyond 64^3. Even at 32^3 resolution, where KECons under-predicts peak dissipation by 14%, it still reaches peak dissipation at the expected time of $t \approx 8$. At 256^3 resolution, the small differences between the incompressible DNS and KECons can be attributed to compressibility effects and the non-zero bulk viscosity $\beta = -2\mu/3$. It also produces visually satisfying results as can be seen in figure 7, where all the vortical structures are smooth and well-defined.

Results for other schemes are shown in figure 8 at a resolution of 64^3 where KECons already correctly predicts peak dissipation. WENO6 produces excessive dissipation early on, with marked departures from the benchmark as early as $t = 3$. On the other hand, the Central6 scheme provides more gentle dissipation from the start. Even at 32^3 resolution, KECons arguably performs better than WENO6 at 64^3, which over-predicts the dissipation peak by 19% and departs significantly from the benchmark as early as $t = 3$.

4.5 Turbulent Channel Flow

Turbulent channel flow is one of the critical tests that measures a solver's ability to capture wall-bounded, highly anisotropic boundary layer physics. In this context, the goal of LES is to recover first order statistics of DNS and experiments at a fraction of the computational cost by coarsening the grid in all directions.

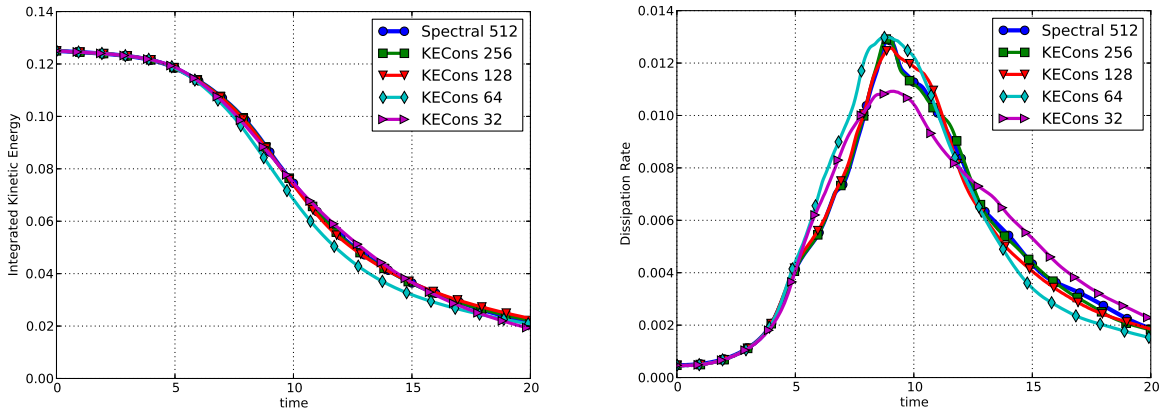

(a) $E_k(t) = \rho u_i u_i/2$ (b) $-\frac{\partial E_k}{\partial t}$

Figure 6: Taylor-Green Vortex results for kinetic energy conserving scheme (KECONS) with the dynamic σ SGS model at different grid resolutions

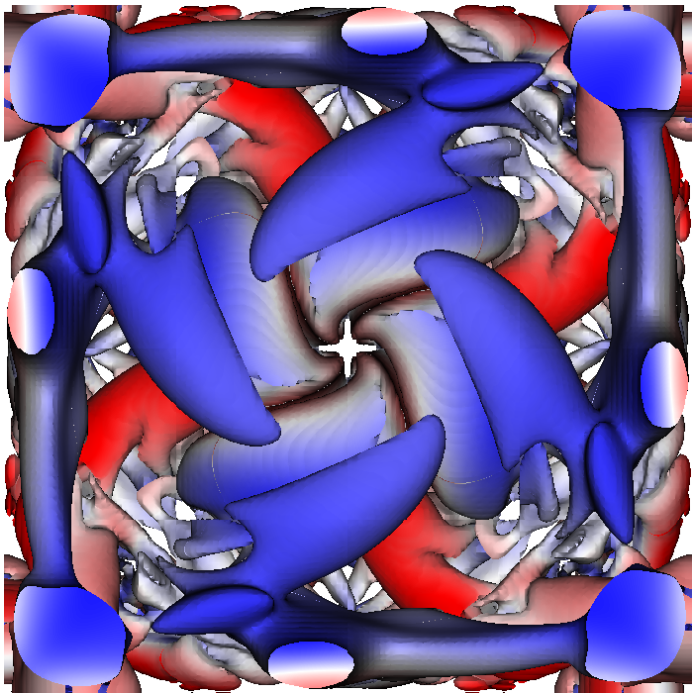

Figure 7: Iso-surfaces of Q-criterion = 1.5 at $t = 8.04$ colored by velocity magnitude for KECons with 256^3

The bulk Reynolds number is set to $R_b = \rho U_0 \delta/\mu = 3300$, and the friction Reynolds number to $Re_\tau = \rho u_\tau \delta/\mu = 180$. A constant body force $F_b = \rho u_\tau^2/\delta$ is used to prevent the flow from decaying to a stop. To keep compressibility effects at a minimum while allowing a larger time step, the Mach number is set to $M_0 = 0.2$. The channel centerline velocity U_0 is set to 1, density ρ is set to 1 and the gas is air with $\gamma = 1.4$. The domain spans $[6.1875, 2.0625, 3.09375]$ channel half-widths δ in the x, y and z directions respectively. It is discretized using 64 evenly distributed cells in each direction, giving a cell size in inner units of $\Delta x^+ = 17, \Delta y^+ = 5.8, \Delta z^+ = 8.7$ with the first cell center inside the channel at $\Delta y^+ = 2.9$. This corresponds to less than half the resolution required for the benchmark DNS in each direction [22], and roughly 6.6% of the overall number of points. The time step is set to $\Delta t = 0.0025$ to keep the CFL near

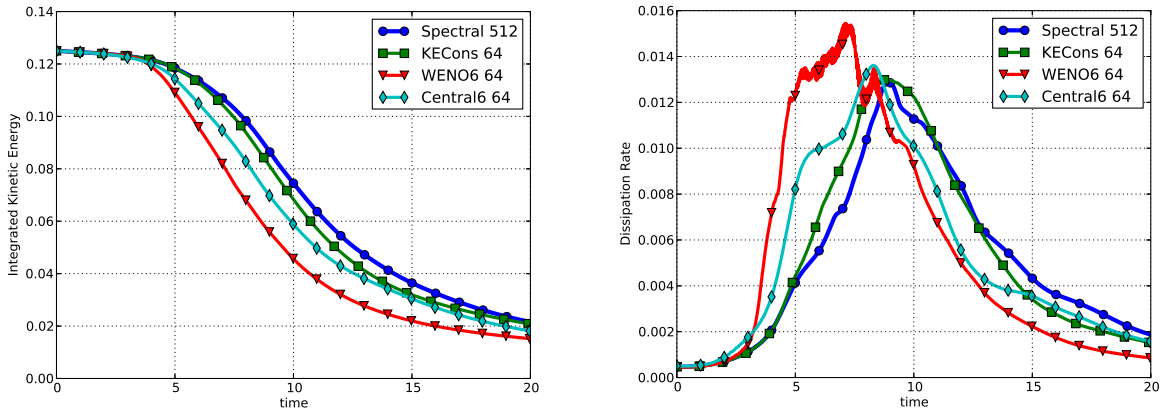

(a) $E_k(t) = \rho u_i u_i/2$ (b) $-\frac{\partial E_k}{\partial t}$

Figure 8: Taylor-Green Vortex results for kinetic energy conserving scheme (KECONS) with the dynamic σ SGS model compared to ILES with different finite difference schemes at 64^3 resolution

0.5, and the flow is integrated in time using explicit RK4 for 167 flow-through times. Statistics are gathered over the last 100 flow-through times.

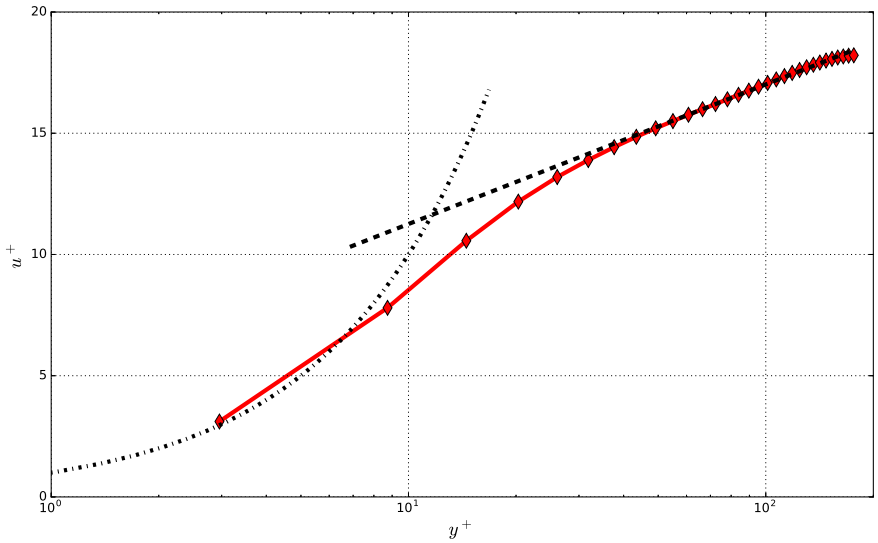

Figure 9: Mean velocity profile for channel flow at $Re_\tau = 180$: KECons 64^3 (diamonds), law of the wall $u^+ = 2.5\ln(y^+) + 5.5$ (dashes), $u^+ = y^+$ (dash-dots).

Figure 9 shows the obtained time and planar averaged velocity profile in non-dimensionalized by the friction velocity u_τ. Despited having only two points below $y^+ = 10$, the mean velocity profile agrees well with the linear law of the wall in the inner viscous layer. In the logarithmic region, near perfect agreement is found with the low-Reynolds number law of the wall, where the offset is increased from 5 to 5.5 [22]. The root-mean-square velocity fluctuations agree well with both DNS and experiment as demonstrated by figure 10. The slight over-prediction of u^+_{rms} and under-prediction of w^+_{rms} in the buffer region and logarithmic region compared to DNS is a common occurrence when the vertical direction is under-resolved. These results are particularly encouraging for the prospect of accurately predicting higher Reynolds number wall-bounded

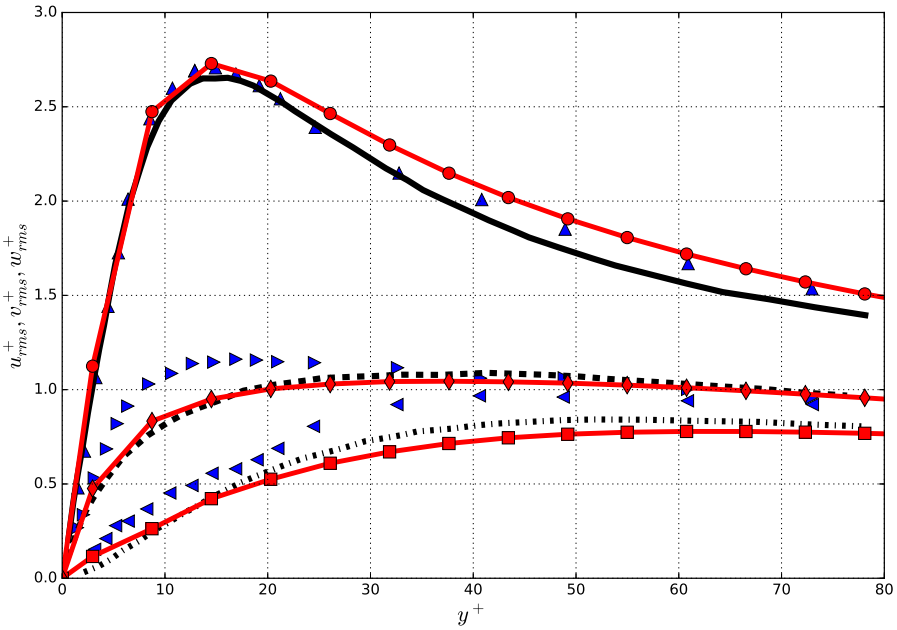

Figure 10: Root-mean-square velocity fluctuations for channel flow at $Re_\tau = 180$. Kreplin & Eckelmann (1979) corrected experimental data [22]: u^+_{rms} (triangles), v^+_{rms} (right triangles), w^+_{rms} (left triangles); DNS [22]: u^+_{rms} (line), v^+_{rms} (dashes), w^+_{rms} (dash-dots); KECons 64^3: u^+_{rms} (circles), v^+_{rms} (diamonds), w^+_{rms} (squares).

flows with a similar number of grid points by using a wall model.

4.6 Flow Past Cylinder

Flow over a cylinder at $Re_D = 3900$ is a well-established unsteady benchmark for low Mach number LES for which there is experimental data available. The goal is to correctly predict the mean velocity profiles across the wake at different downstream stations ranging from 1 to 6 cylinder diameters. The cylinder is placed at the origin and has a diameter D, which will henceforth be used to non-dimensionalize all lengths. The domain spans $[-6, -8, -2]$ to $[26, 8, 2]$ in x, y, z respectively, where x is the flow direction, y the vertical direction and z the spanwise direction. The upstream boundary condition is prescribed to be the reference velocity and pressure, whereas the downstream domain boundary is treated as a subsonic outflow (pressure is set, all other primary variables are extrapolated from the interior) boundary condition. Periodicity is enforced both in the vertical and in the spanwise directions. Enforcing periodicity in the vertical is equivalent to an infinite array of cylinders 8 D apart as opposed to a single one in freestream. This approach allows us to reduce the size of the domain without incurring strong confinement effects. This problem tests the ability of the proposed scheme to deal with immersed boundaries accurately, and transition from laminar to turbulent flow in the wake.

Figure 11 shows the mesh used for KECons. Each level of refinement visible in figure 11 corresponds to a factor of 2 in each direction. The coarsest level extends the entire domain, whereas the finest level of resolution $\Delta x = 1/64$ is reserved only for the geometry to ensure that the effects of curvature are resolved by the GCM. This is important for this kinetic energy conserving scheme where we observe secondary instabilities on the shear layer much earlier when the curvature of the geometry is not as smoothly represented by the GCM. Immediately outside of the vicinity of the cylinder, the mesh size increases to $\Delta x = 1/32$. The entire mesh is 8 million cells, not counting ghost cells necessary for parallelization and coarse-fine interfaces.

Shedding occurs and the remnants of a transitional Von-Karman vortex street are visible. This is exem-

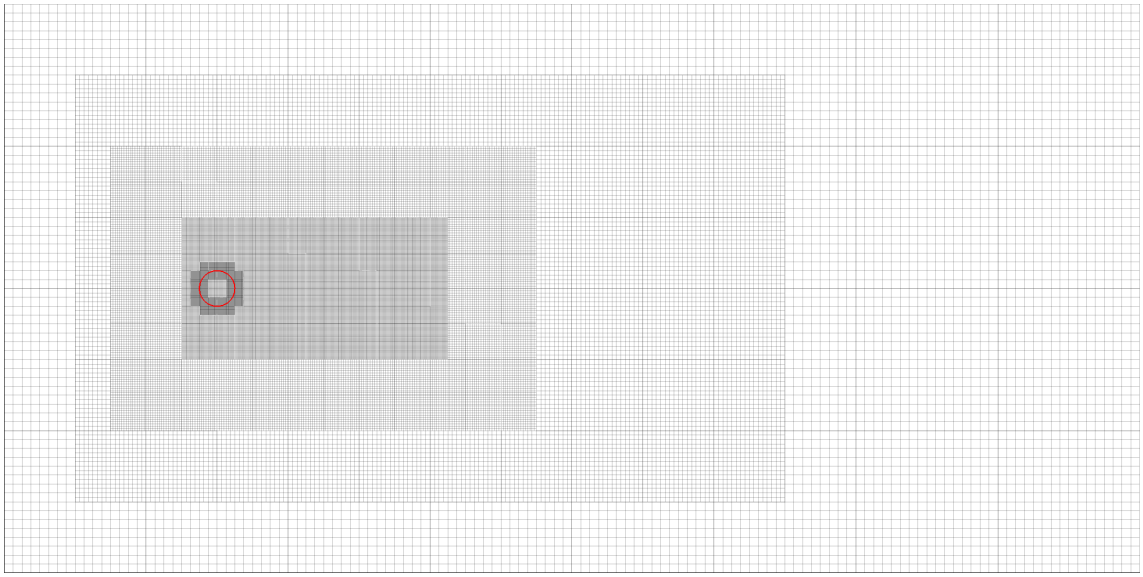

Figure 11: Slice of the mesh showing an $x-y$ plane for flow past cylinder at $Re_D = 3900$.

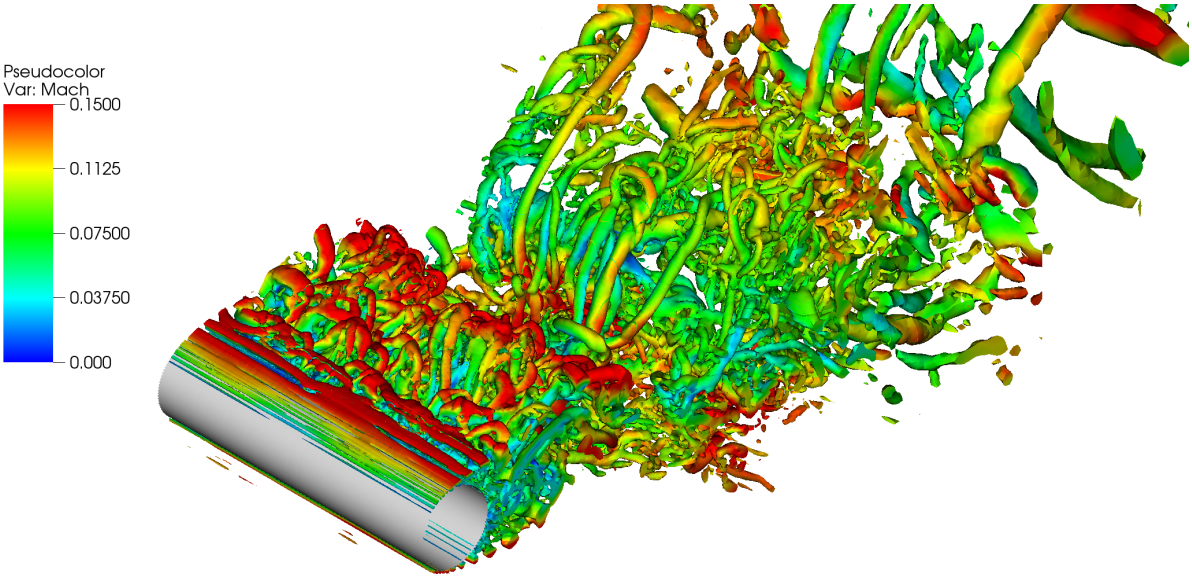

Figure 12: Instantaneous snapshot of iso-surfaces of Q-criterion colored by Mach number for flow past cylinder at $Re_D = 3900$.

plified in figure 12, where the iso-surfaces of the Q-criterion delineate the turbulent structures and coherent vortex cores. Results are time-averaged over the last 26 shedding periods and compared to benchmark experimental, DNS, and LES data in figure 13. The KECons mean velocity profiles agree very well with the benchmark data at all locations except near $x/D = 2$ where both KECons and WENO6 have a smaller velocity deficit.

This is likely due to the coarseness of the grid and its inability to represent the geometry with high fidelity. The flow thus sees a bumpier geometry, and transitions earlier than expected. As soon as 3D turbulent structures appear, both the σ SGS model in the case of KECons, and the smoothness indicator in the case of WENO6 are triggered as expected, providing further dissipation and increased mixing, which would explain the wider velocity profile and smaller velocity deficit. From $x = 3$ to $x = 5$, KECons recovers

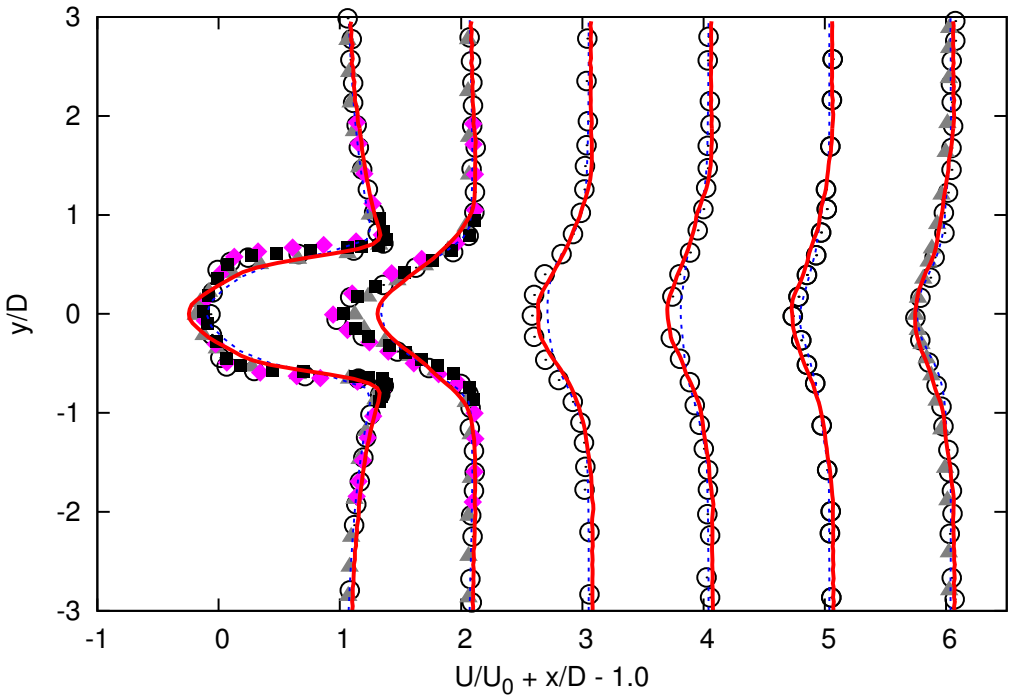

Figure 13: Time-averaged velocity profiles for flow past a cylinder at $Re_D = 3900$. Experimental PIV Measurements [23] (squares), DNS at $Re = 3300$ [24] (circles), LES [23] (triangles), LES [25] (diamonds), LAVA WENO6 (dashes), LAVA KECons + σ model (line).

the DNS data accurately, whereas the WENO6 seems to provide excessive dissipation and has a lower velocity deficit. Downstream of $x = 5$, both KECons and WENO6 show good agreement with the DNS and LES benchmarks. This confirms that the limiting factor for the new KECons algorithm is the geometry representation. Without resorting to a more costly and complex immersed-boundary method, the only resort is to increase the grid resolution near the geometry.

5 Conclusions and Future Work

We proposed a novel high-order finite difference scheme to solve the Navier-Stokes equation that conserves kinetic energy in space and in time that is well-suited to perform explicit LES. Its implementation into the Cartesian immersed boundary solver of the Launch, Ascent, and Vehicle Aerodynamics (LAVA) framework [8] was presented. The scheme was shown to provide the expected convergence rate using the method of manufactured solutions (MMS), and to have increased stability properties which allow it to perform well on the isentropic vortex problem without the addition of any numerical dissipation. It conserved kinetic energy in space and in time for the (small) time steps tested regardless of whether the more expensive symplectic time integrator was used in both the isentropic vortex propagation and inviscid Taylor-Green vortex benchmark problems. Its ability to perform large-eddy simulation (LES) with increased accuracy was demonstrated on the Taylor-Green vortex at $Re = 1600$, where it captures the dissipation peak at only 64^3 resolution. LES of turbulent channel flow was also performed and displayed good agreement with benchmark data, showing the scheme's ability to deal with highly anisotropic wall-bounded turbulence. Finally, flow past a cylinder at $Re_D = 3900$ was simulated to verify the proposed algorithm's coupling with the ghost cell method (GCM), and its performance when dealing with under-resolved geometry. Obtained results agreed well with the benchmarks and confirmed that the geometry representation is now the limiting factor.

Future work will focus on three fronts. The first effort will be to implement shock-capturing capability to enable the simulation of rotorcraft and of high speed jet acoustics. We will also invest in the development

of robust turbulent wall-layer modeling in order to simulate wall-bounded flow with complex geometries for target applications like flap noise. The last focus will be to implement better thin and highly curved geometry representation through a higher-order immersed boundary method.

Acknowledgments

This work was funded by the NASA Transformational Tools and Technologies Project (T^3) of the Transformative Aeronautics Concepts Program under the Aeronautics Research Mission Directorate (ARMD). Computer time has been provided by the NASA Advanced Supercomputing (NAS) facility at NASA Ames Research Center. We would like to thank our colleagues in the Computational Aerosciences branch for many useful discussions on the topic and for valuable feedback.

References

[1] Jeffrey Slotnick, Abdollah Khodadoust, Juan Alonso, David Darmofal, William Gropp, Elizabeth Lurie, and Dimitri Mavriplis. CFD vision 2030 study: a path to revolutionary computational aerosciences. *NASA Technical Report*, 2014.

[2] F.E. Ham, F.S. Lien, and A.B. Strong. A fully conservative second-order finite difference scheme for incompressible flow on nonuniform grids. *J. Comp. Phys.*, 177(1):117 – 133, 2002.

[3] Felix S. Schranner, J. Andrzej Domaradzki, Stefan Hickel, and Nikolaus A. Adams. Assessing the numerical dissipation rate and viscosity in numerical simulations of fluid flows. *Computers & Fluids*, 114(0):84 – 97, 2015.

[4] G. Castiglioni and J.A. Domaradzki. A numerical dissipation rate and viscosity in flow simulations with realistic geometry using low-order compressible Navier-Stokes solvers. *Computers & Fluids*, 119:37 – 46, 2015.

[5] F. Cadieux, G. Sun, and J.A. Domaradzki. Effects of numerical dissipation on the interpretation of simulation results in computational fluid dynamics. *Computers & Fluids*, 119:37 – 46, 2017.

[6] Yohei Morinishi. Skew-symmetric form of convective terms and fully conservative finite difference schemes for variable density low-mach number flows. *Journal of Computational Physics*, 229(2):276–300, 2010.

[7] Jens Brouwer, Julius Reiss, and Jorn Sesterhenn. Conservative time integrators of arbitrary order for skew-symmetric finite-difference discretizations of compressible flow. *Computers & Fluids*, 100:1 – 12, 2014.

[8] Cetin C Kiris, Jeffrey A Housman, Michael F Barad, Christoph Brehm, Emre Sozer, and Shayan Moini-Yekta. Computational framework for launch, ascent, and vehicle aerodynamics (lava). *Aerospace Science and Technology*, 55:189–219, 2016.

[9] Yuichi Kuya and Soshi Kawai. Physically consistent formulations for kinetic energy preservation by quasi-skew-symmetric forms. In *2018 AIAA Aerospace Sciences Meeting*, page 1563, 2018.

[10] Sergio Pirozzoli. Numerical methods for high-speed flows. *Annual Review of Fluid Mechanics*, 43(1):163–194, 2011.

[11] Franck Nicoud, Hubert Baya Toda, Olivier Cabrit, Sanjeeb Bose, and Jungil Lee. Using singular values to build a subgrid-scale model for large eddy simulations. *Phys. Fluids*, 23(8):–, 2011.

[12] Jungil Lee, Haecheon Choi, and Noma Park. Dynamic global model for large eddy simulation of transient flow. *Physics of Fluids*, 22(7):075106, 2010.

[13] Ali Mani. Analysis and optimization of numerical sponge layers as a nonreflective boundary treatment. *Journal of Computational Physics*, 231(2):704–716, 2012.

[14] Thomas Pulliam. High order accurate finite-difference methods: as seen in overflow. In *20th AIAA Computational Fluid Dynamics Conference*, page 3851, 2011.

[15] Rajat Mittal, Haibo Dong, Meliha Bozkurttas, FM Najjar, Abel Vargas, and Alfred von Loebbecke. A versatile sharp interface immersed boundary method for incompressible flows with complex boundaries. *Journal of computational physics*, 227(10):4825–4852, 2008.

[16] Ken Mattsson and Martin Almquist. A high-order accurate embedded boundary method for first order hyperbolic equations. *Journal of Computational Physics*, 334:255–279, 2017.

[17] Kazuhiro Nakahashi. Immersed boundary method for compressible euler equations in the building-cube method. In *20th AIAA Computational Fluid Dynamics Conference*, page 3386, 2011.

[18] Carlos Pantano, Ralf Deiterding, David J Hill, and Dale I Pullin. A low numerical dissipation patch-based adaptive mesh refinement method for large-eddy simulation of compressible flows. *Journal of Computational Physics*, 221(1):63–87, 2007.

[19] Daniel J Bodony, George Zagaris, Adam Reichert, and Qi Zhang. Provably stable overset grid methods for computational aeroacoustics. *Journal of Sound and Vibration*, 330(17):4161–4179, 2011.

[20] Christoph Brehm, Michael F Barad, Jeffrey A Housman, and Cetin C Kiris. A comparison of higher-order finite-difference shock capturing schemes. *Computers & Fluids*, 122:184–208, 2015.

[21] Antony Jameson. Evaluation of fully implicit runge kutta schemes for unsteady flow calculations. *Journal of Scientific Computing*, 73(2-3):819–852, 2017.

[22] John Kim, Parviz Moin, and Robert Moser. Turbulence statistics in fully developed channel flow at low reynolds number. *Journal of fluid mechanics*, 177:133–166, 1987.

[23] Philippe Parnaudeau, Johan Carlier, Dominique Heitz, and Eric Lamballais. Experimental and numerical studies of the flow over a circular cylinder at reynolds number 3900. *Physics of Fluids*, 20(8):085101, 2008.

[24] JG Wissink and W Rodi. Numerical study of the near wake of a circular cylinder. *International journal of heat and fluid flow*, 29(4):1060–1070, 2008.

[25] Arthur G Kravchenko and Parviz Moin. Numerical studies of flow over a circular cylinder at re d= 3900. *Physics of fluids*, 12(2):403–417, 2000.